Bulk-like transverse electron mobility in an array of heavily *n*-doped InP nanowires probed by terahertz spectroscopy

C. S. Ponseca, Jr.,[1,*] H. Němec,[2,*] J. Wallentin,[3,†] N. Anttu,[3] J. P. Beech,[3] A. Iqbal,[1] M. Borgström,[3] M.-E. Pistol,[3] L. Samuelson,[3] and A. Yartsev[1]

[1]*Department of Chemical Physics, Lund University, Getingevägen 60, Box 124, 221 00 Lund, Sweden*

[2]*Institute of Physics of the Academy of Sciences of the Czech Republic, Na Slovance 2, 182 21 Praha 8, Czech Republic*

[3]*Division of Solid State Physics, Lund University, Box 118, Lund S-22100, Sweden*

(Received 28 November 2013; revised manuscript received 18 July 2014; published 5 August 2014)

Terahertz spectroscopy is employed for the noncontact measurement of transversal mobility in InP nanowires, wherein photonic effects (waveguiding of excitation beam and propagation of terahertz beam in a complex gradient environment) were successfully deconvoluted. Monte Carlo calculations accounting for electron localization and heavy doping were used to determine electron momentum relaxation time corresponding to electron mobility $\geq$3000 cm^2/V s, which is similar to that in bulk InP. The developed approach paves a way for noncontact determination of charge mobility in advanced semiconductor nanostructures.

DOI: 10.1103/PhysRevB.90.085405 PACS number(s): 78.67.Uh, 72.20.−i, 73.23.−b, 78.47.J−

I. INTRODUCTION

Terahertz (THz) electromagnetic radiation interacts strongly with free charge carriers [1], thus providing a noncontact tool for the measurement and characterization of charge transport properties in bulk semiconductors [2]. In the linear conductivity regime, the probed characteristic transport length scale $L_\omega = \sqrt{D/\omega}$ depends on the probing angular frequency ω and on the diffusion coefficient D of charges [3]. While dc conductivity reflects long-range transport processes, high-frequency conductivity carries information on the nanoscale motion ($L_{1\,\mathrm{THz}} = 47$ nm in InP), which makes THz spectroscopy suitable for the investigation of charge transport and dynamics in semiconductor nanostructures. The charge mobility in nano-objects reflects both the quality of the nanocrystal (represented by charge carrier scattering processes) and the carrier confinement (due to interactions with nanocrystal boundaries). Optimization of the former process is a crucial task in nanotechnologies for optoelectronics: It is important to analyze the carrier scattering in nanostructures and compare it with transport in bulk of the same materials as it gives a benchmark for determining the efficiency of the charge transport in the nanostructures. Characterization of mobility in nanostructures is very challenging using conventional methods such as Hall effect measurements: namely, nanometer-sized electrodes need to be attached to the nanostructure; data analysis is complicated by fringe capacitance due to the contacts and the results are influenced also by the extent of the depletion region [4]. Here we show that terahertz spectroscopy is a powerful alternative to conventional methods, which makes contact-free determination of charge mobility and carrier scattering time in ensembles of nanostructures feasible. To fully profit from this method, several phenomena governing THz spectra have to be analyzed carefully.

The inherent inhomogeneity of semiconductor nanostructures imposes several challenges in obtaining charge transport properties from THz spectra. Charge confinement effects at THz frequencies are usually neglected in structures with sizes exceeding tens of nanometers. We will show that due to the long characteristic transport lengths L_ω in high-mobility semiconductors, charge confinement effects at THz frequencies need to be considered even for dimensions of hundreds of nanometers [5,6]. Furthermore, the measured (effective) THz conductivity (defined as the response to the *applied* THz field) in inhomogeneous structures essentially differs from the microscopic conductivity of individual nano-objects (defined as the response to the *local* THz field) due to the presence of depolarization fields [7,8]. A careful evaluation of the role of these fields is a prerequisite for the correct determination of the carrier mobility in structured materials [6,9–15]. Additionally, resonant enhancement of optical absorption in structures with characteristic dimensions comparable to the optical wavelength [16] is closely related to a complex spatial distribution of the absorbed energy [17]. The corresponding inhomogeneity in the charge density further modifies the depolarization fields.

Some of these effects have been to a certain extent addressed individually in the past. For example, Johnston's group performed a notable series of investigations of a variety of nanowires (NWs) with sub-100 nm diameters. Using solely effective medium approximation, they analyzed THz spectra and determined charge carrier mobilities [10–14]. The rubbing technique used to prepare those samples did not allow a full control over the morphology; namely, the transversal and longitudinal response was likely to mix due to the random orientation of the NWs. The influence of inhomogeneous photoconductivity on THz response has been often neglected despite the fact that even a linear absorption leads to a nontrivial THz beam propagation in photoexcited semiconductor nanostructures [9]. The influence of charge localization has been frequently studied using phenomenological models [18], which offer a limited connection to microscopic properties [19]. The microscopic models developed so far are restricted to nondegenerate semiconductors (low excitation and doping densities) [5,20], whereas the response is altered

*These authors contributed equally to this work: carlito.ponseca@chemphys.lu.se and nemec@fzu.cz.

†Current address: Institute for X-ray Physics, University of Göttingen, Friedrich-Hund-Platz 1, 37077 Göttingen, Germany.

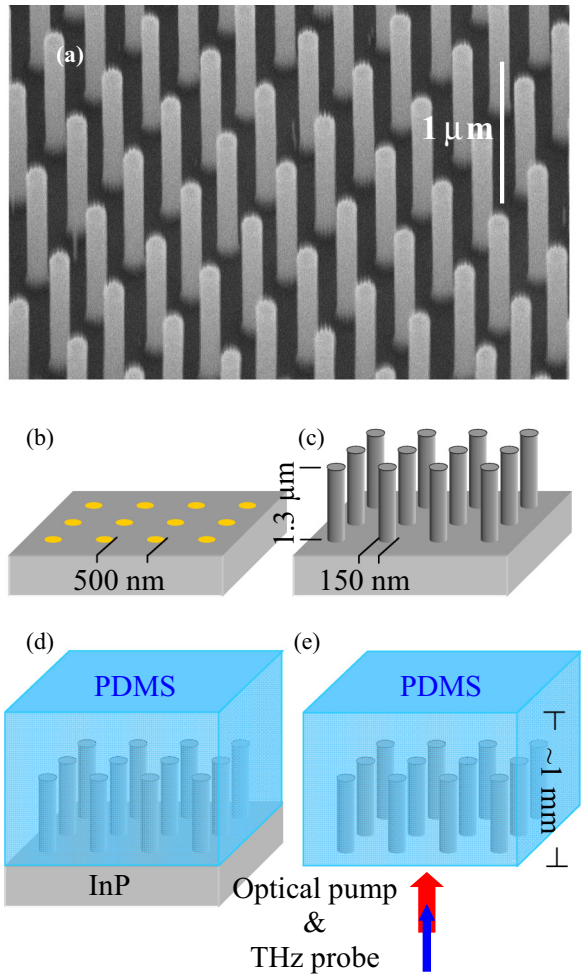

FIG. 1. (Color online) (a) SEM image of the NWs grown on the InP substrate. (b)–(e) Fabrication of the investigated sample and sketch of the geometry of the pump-probe experiment. Both THz and excitation beam propagate along the NW axis.

as the Fermi velocity increases due to increasing charge density.

In this work we investigate InP NWs with diameter $d = 150$ nm and length 1.3 μm, doped by Sn to the level of 5×10^{18} cm^{-3} [Fig. 1(a)]. We take into account *all* the above-mentioned effects; this is required due to the specific dimensions and doping levels of the NWs. This allows us to determine the electron scattering time and the corresponding transversal electron mobility in the array of vertically aligned NWs.

II. SAMPLE PREPARATION

Substrates of p^+-InP (111)B (Zn-doped to 5×10^{18} cm^{-3}) were prepared for NW growth by nano imprint lithography, metal evaporation, and lift-off of 30 nm Au films creating a pattern with 180 nm gold dots with a pitch of $a = 500$ nm arranged in a periodic pattern [Fig. 1(b)]. NWs were subsequently grown in a low-pressure (100 mbar) metal organic vapor phase epitaxy (MOVPE) system (Aixtron 200/4) using hydrogen (H_2) as carrier gas with a total flow of 13 l/min [Fig. 1(c)]. For InP growth, trimethylindium (TMI) and phosphine (PH_3) were used as precursors, with constant molar fractions of $\chi_{TMI} = 30.7 \times 10^{-6}$ and $\chi_{PH3} = 6.9 \times 10^{-3}$. Tetraethyltin (TESn) was used as the n-dopant precursor [21]. Hydrogen chloride (HCl) at a molar fraction of $\chi_{HCl} = 4.6 \times 10^{-5}$ was used to control the radial growth [22]. The samples were first annealed at 550 °C for 10 min under a PH_3/H_2 gas mixture to desorb any surface oxides. The reactor was then cooled to 440 °C, at which growth was initiated by adding TMI to the gas flow. After a 15 s nucleation time, HCl was introduced, simultaneously with the dopant, resulting in a nominal acceptor concentration of about 5×10^{18} cm^{-3} [23]. Then NWs were grown for 17 min, after which the growth was terminated by switching off the group III, HCl, and where the dopant flows and cooling down the samples in a PH_3/H_2 gas mixture. Finally, polydimethylsiloxane (PDMS) was poured onto the substrate and after curing the substrate was removed, leaving the oriented NWs inside PDMS matrix [Figs. 1(d) and 1(e)].

III. THEORY

We employ finite element method (COMSOL Multiphysics) to calculate the distribution of the excitation density [Figs. 2(a) and 2(b)] in a periodic array of NWs embedded in a semi-infinite slab of PDMS [24] (optical properties of InP were taken from Ref. [29]). Although this distribution is strongly inhomogeneous at the time of the photoexcitation, it rapidly smoothes with time due to diffusion and the density redistributes on the hundreds of nanometers length scale [25]. It is then natural to average the excitation density in planes orthogonal to the NW axis; the longitudinal profile can be subsequently approximated by an exponential decay given by an effective absorption coefficient α_{eff} [Fig. 2(c); the definition of α_{eff} is further commented in Appendix A; symbol meanings are summarized in Appendix B] which is calculated from the fraction of energy absorbed in the entire NW:

$$n_{\text{exc}}(z) = H_{\text{p}} \frac{\alpha_{\text{eff}}}{s} \exp(-\alpha_{\text{eff}} z), \tag{1}$$

where H_{p} is the incident photon exposure per laser pulse (in photons/cm^2; charges are assumed to recombine prior to the arrival of the next laser pulse) and $s = \pi d^2/4a^2 = 7\%$ is the filling factor of the NWs. Using this definition, the ratio $\beta = \alpha_{\text{eff}}/(s\alpha)$ describes the enhancement of the absorption (per absorbing material volume) due to waveguiding effects, compared to the absorption coefficient of bulk InP, α [Fig. 2(c)].

The comparatively weak absorption at longer wavelengths ($\lambda_{\text{exc}} \gtrsim 550$ nm) enables interference of light inside the NWs and leads to the resonant enhancement of effective optical absorption for our NW diameter and wavelength range [16]. Conversely, for shorter wavelengths ($\lambda_{\text{exc}} \lesssim 550$ nm), the absorption length of bulk InP is very short compared to the dimensions of the NWs. Therefore, such photons are absorbed mainly at the NWs surface and interact more weakly with the NWs than do the long-wavelength photons. Since only a small fraction of the short-wavelength photons is absorbed near the surface along the length of the NWs [Fig. 2(a)], the effective absorption is strongly suppressed.

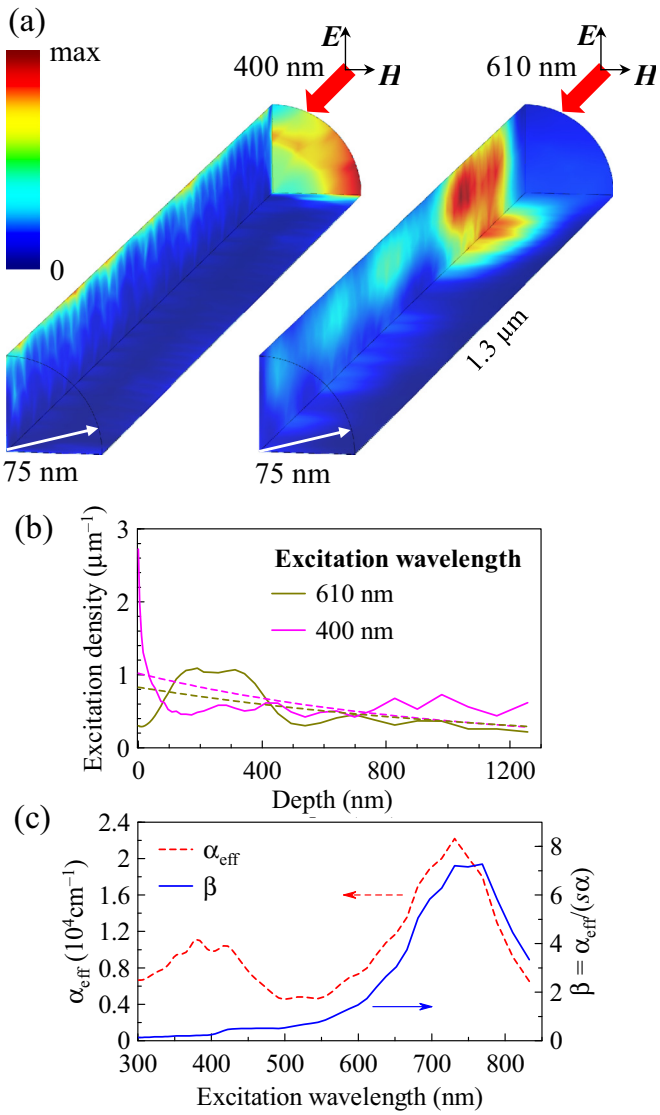

FIG. 2. (Color online) (a) Calculated distribution of the excitation density (number of photons absorbed in a unit volume) in the NW induced by a polarized light beam. The densities are plotted in a section of the NWs for the two excitation wavelengths employed in the experiments. (b) Relative excitation density integrated over the circular cross section of the nanowires. Solid lines: Calculation by COMSOL Multiphysics (before the diffusion becomes effective). Dashed lines: Approximation using an effective absorption coefficient. (c) Effective absorption coefficient and absorption enhancement factor β as a function of the excitation wavelength, determined from the calculations by COMSOL Multiphysics.

We measured transient THz transmittance spectra of the NWs $\Delta T/T$ in order to determine their effective transient sheet photoconductivity $\Delta\Sigma_{\rm eff}$ [9,19]:

$$\frac{\Delta T}{T}(\omega) = -\frac{Z_0}{2n}\Delta\Sigma_{\rm eff}(\omega), \tag{2}$$

where Z_0 is the vacuum impedance and n is the refractive index of the material surrounding the photoconducting layer. Since time-resolved THz spectroscopy is a phase-sensitive technique, both real and imaginary parts of the transmittance and all derived conductivities are obtained. Note that the probe beam polarization is orthogonal to the NW axis so that we probe the transversal conductivity, not that along the growth axis.

The wavelength of the THz radiation (>0.12 mm) is much longer than the period a of the NW array, implying that the effective conductivity $\Delta\sigma_{\rm eff}$ can be calculated from the microscopic conductivity $\Delta\sigma$ using an effective medium approximation. Since the NWs in the array are sparse, Maxwell-Garnett effective medium approximation applies, resulting in [6,9]

$$\Delta\sigma_{\rm eff}(z,\omega) = \frac{B\Delta\sigma(z,\omega)}{1 + iD\Delta\sigma(z,\omega)/(\omega\varepsilon_0)}, \tag{3}$$

where the constants B and D reflect the filling factor of the photoconducting component s, depolarization factor of the NWs, and the equilibrium permittivities of the sample:

$$B = \frac{\varepsilon_m(1+sK) - \varepsilon_{\rm eff}(1-s)}{\varepsilon_m(s+K) + \varepsilon_{\rm NW}(1-s)},$$
$$D = \frac{(1-s)}{\varepsilon_m(s+K) + \varepsilon_{\rm NW}(1-s)}.$$

The derivation is described in Ref. [19]; $K = 1$ is the depolarization factor for cylindrical shape, $\varepsilon_{\rm m} = 2$ is the permittivity of the polymer matrix, $\varepsilon_{\rm NW} = 12.5$ is the permittivity of the NWs (without photoexcitation), and $\varepsilon_{\rm eff} = 2.2$ is the effective permittivity of the layer with NWs.

The effective sheet conductivity is obtained by integrating over the thickness L of the layer with the NWs:

$$\Delta\Sigma_{\rm eff} = \int_0^L \Delta\sigma_{\rm eff}(z)dz. \tag{4}$$

Since electrons have higher mobility than holes in InP, we assume that the microscopic transient conductivity $\Delta\sigma(\omega,z) = e_0\varphi n_{\rm exc}(z)\mu(\omega)$ is proportional to the product of the quantum yield of charge-pair generation φ and the electron mobility spectrum $\mu(\omega)$. Combining Eqs. (1)–(4) then results in the model function for the transient transmittance spectrum:

$$\frac{\Delta T}{T}(\omega) = -\frac{Z_0 e_0 H_{\rm p} B}{2ns\beta}\frac{\ln\frac{1+iu(\omega)D\beta\varphi\mu(\omega)}{1+iu(\omega)D\beta\varphi\mu(\omega)\exp(-\alpha\beta sL)}}{iu(\omega)D}, \tag{5}$$

where $u(\omega) = e_0 H_{\rm p}\alpha/(\omega\varepsilon_0)$. This formula reflects the tangled depth profile of the effective conductivity and it is discussed in detail in Ref. [19]. Most parameters in Eq. (5) represent the properties of bulk InP or stem directly from the morphology of the sample (α, β, n, s, L and the derived parameters B and D). The quantum yield φ of electron generation and the electron mobility spectrum $\mu(\omega)$ are the only unknowns.

For very low excitation densities, the photoconductivity is weak and it affects the depolarization fields in a perturbative way only [6]. Equation (5) then reduces to

$$\frac{\Delta T}{T}(\omega) = -\frac{Z_0 e_0 H_{\rm p} B}{2ns}\varphi\mu(\omega)[1 - \exp(-\alpha\beta sL)], \tag{6}$$

which—apart from the structure-related factor B/s—is the same as in the case of a homogeneous thin film [19]. This linear relationship between transient transmittance and mobility (Fig. 3) is favorable for the determination of the mobility spectrum, and in turn, for the assessment of charge transport

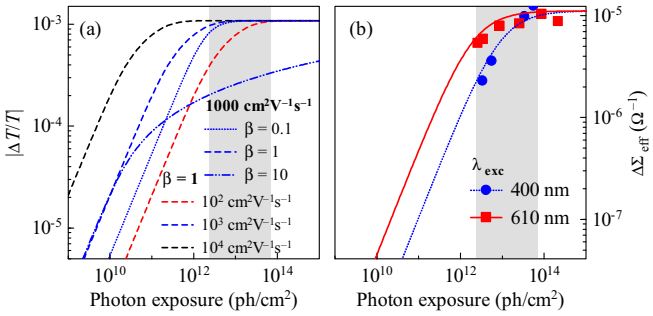

FIG. 3. (Color online) (a) Calculated transient THz transmittance versus excitation photon exposure for various real-valued mobilities μ and absorption enhancement factors β at $f = 1$ THz ($\varphi = 1$, $\alpha = 10^7$ m^{-1}). The shape of the curve is changing with increasing β due to the increasing importance of the nonlinearity originating from Eq. (3). The shaded area represents excitation fluences used in the measurements. (b) The same dependence corresponding to the system under the study for both excitation wavelengths ($f = 1$ THz). Lines are calculated based on the parameters of fits over the entire spectral range (Fig. 4) and symbols represent measured data.

properties in the NWs. However, it is very difficult to experimentally attain this regime in diluted systems as the required low excitation photon exposures yield extremely weak signals (notice the $\Delta T/T$ scale in Fig. 3). In the opposite limit (high excitation densities), a plasmonic resonance develops and blueshifts with increasing excitation density [6,8,10–14]. This latter regime is described by the ln term in Eq. (5) and it is characterized by a very weak dependence of the transient transmittance $\Delta T/T$ on the excitation density and on the charge mobility μ (Fig. 3) [6]. The signal then saturates in the limit of perfectly conducting cylinders ($F \to \infty$):

$$\frac{\Delta T}{T}(\omega) = -\frac{i\omega L B}{2nc}, \tag{7}$$

which reflects the fact that information on the charge mobility is encoded namely in the spectrum close to the resonance, which is shifted above the accessible spectral region in this regime. Here we operate in an intermediate regime, which constitutes a compromise allowing us to both spectrally resolve the microscopic response and to observe the signal with an acceptable noise level.

IV. RESULTS AND DISCUSSION

The transient THz transmittance was measured in a standard setup [1] based on a femtosecond Ti:sapphire amplifier (Spitfire, 800 nm, 80 fs pulse length, 1 kHz repetition rate), where the THz pulses were generated by optical rectification and detected via electro-optic sampling in (110) ZnTe crystals.

For the highest excitation fluences, the magnitude of the imaginary part of the transient conductivity is much larger than the real part and the $\Delta T/T$ spectra are almost independent of the excitation fluence (Fig. 4). This corresponds to the high-fluence regime [Eq. (7)]. Upon lowering the excitation fluence, $\Delta T/T$ spectra start to change, i.e., the intermediate regime is reached. For the lowest excitation densities, $\Delta T/T$ is approximately proportional to the excitation fluence, indicating that we are close to the regime described by

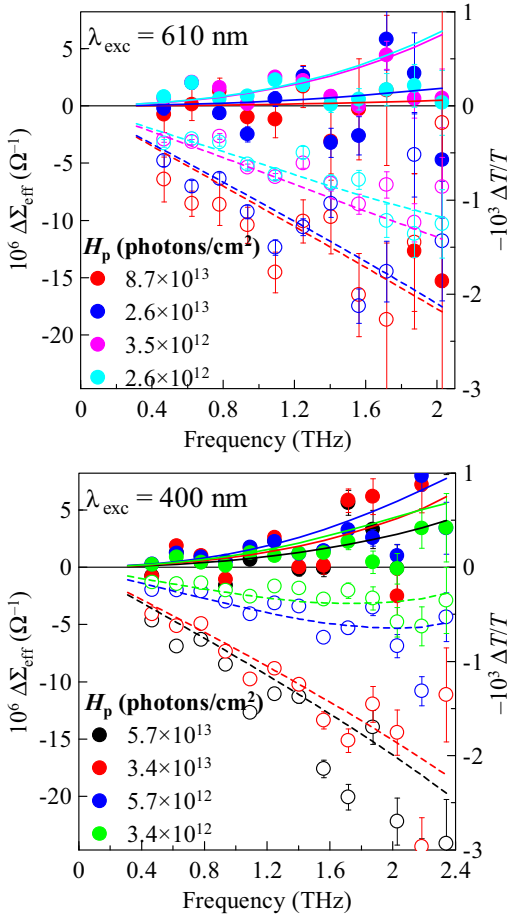

FIG. 4. (Color online) Spectra of transient transmittance in the investigated arrays of InP NWs for both excitation wavelengths and for various excitation photon exposures H_p, measured 10 ps after photoexcitation. Symbols: measurements, lines: fit by the Monte Carlo model from Fig. 5 and including the effects of depolarization fields and waveguiding described by Eq. (5). Solid lines and closed symbols: real part, dashed lines and open symbols: imaginary part.

Eq. (6). The effective conductivity is then directly proportional to the mobility, which allows us to assess the character of the transport directly from the measured data. The observed imaginary part is negative and its magnitude is higher than the real part—these features are in sharp contrast with the Drude model and they indicate confinement of charges in the NWs [5].

This confinement is studied using semiclassical Monte Carlo simulations of thermal motion of charge carriers confined in NWs. Evaluation of the Kubo formula then provides the mobility spectrum of charges. Unlike in Ref. [5], where Maxwell-Boltzmann statistics were considered, here we are dealing with a heavily doped semiconductor with Fermi energy E_F high in the conduction band (the doping density of 5×10^{18} cm^{-3} corresponds to $E_F \sim 0.25$ eV; note that the maximum excitation densities $H_p \alpha_{eff}/s \sim 10^{18}$ cm^{-3} are lower than the doping level) for which Fermi-Dirac statistics must be used [26]. The mobility spectra are further determined by the diameter of NWs, electron scattering time τ_s, effective mass of electrons m^*, and temperature. A

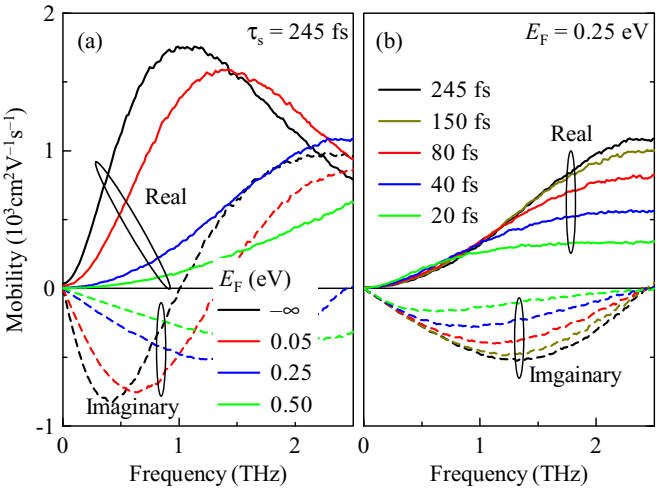

FIG. 5. (Color online) Calculated electron mobility spectra in InP NWs with 150-nm diameter with (a) variable Fermi energy ($-\infty$ corresponds to the Maxwell-Boltzmann distribution) and (b) variable electron mean scattering time.

detailed discussion of the interplay of all these parameters will be covered in a separate article. Here it is important to emphasize that only electrons with energy close to E_F contribute to the conductivity spectrum. Since their mean velocity ($v_F = \sqrt{2E_F/m^*} = 10^6$ m s^{-1}) is significantly higher than the thermal velocity ($v_{therm} = \sqrt{3k_BT/m^*} = 4.1 \times 10^5$ m s^{-1}), the charges more often interact with the NWs surface and the localization effects (appearing as the spectral range with negative imaginary part of conductivity) are then more important even at THz frequencies [Fig. 5(a)]. This effect is analogous to the effect of temperature increase in the case of Maxwell-Boltzmann statistics (Fig. 9 in Ref. [27]). The high number of interaction events with the surface implies that the charge carrier backscattering by the NW surface is more important than the scattering in bulk. Indeed, Fig. 5(b) shows that only a considerable reduction of the scattering time from the bulk value (∼245 fs) leads to important changes of the electron mobility spectra.

The calculated mobility spectra were substituted into Eq. (5) and used for fitting of the measured transient transmittance spectra. We found that the best match is obtained for electron relaxation time τ_s close to the bulk value (lines in Fig. 4). Due to the limited sensitivity of the mobility spectra to this parameter, we can only conclude that τ_s is longer than ∼150 fs ($\mu = e_0\tau_s/m^* \gtrsim 3000$ cm^2 V^{-1} s^{-1}). This means that the *transversal* mobility in the NWs may be lower than in undoped bulk InP (5400 cm^2 V^{-1} s^{-1}), but it is somewhat higher than the dc mobility in a heavily doped InP [28]. This may stem from a different length scale probed by the Hall-effect measurement, or there may be a difference in mobilities of equilibrium and photogenerated charge carriers. Note however, that the *longitudinal* mobility (measured in FET configuration) has been reported almost an order of magnitude lower as stacking faults in the growth direction hinder the longitudinal transport [23]. The fitted quantum yield φ depends on the excitation wavelength: (65 ± 10)% at 610 nm and 14% at 400 nm. These yields are lower than the expected value of 100%, which may be due to rapid surface recombination or absorption in defect states close to the surface. These effects would be more pronounced for the blue excitation where most photons are absorbed within 20 nm from the surface [Figs. 2(a) and 2(b)]. It is noteworthy that a similar trend was observed through the measurement of external quantum efficiency in InP NW solar cells [17].

We should emphasize that there are three physical processes (propagation of the excitation and THz beam, respectively, and confinement of charges), which control the effective conductivity as a function of frequency and excitation density, whereas there are only two parameters (φ and τ_s) adjustable to match a set of several complex transmittance spectra. In this almost overdetermined task, we achieved a very good agreement between calculations and measured spectra in a range spanning 1½ decades of excitation photon exposures. This to a large extent justifies the simplifications made in our description of the processes. For example, the charge carrier density is more complex than the simple exponential profile used to enable analytical calculations of the transient transmittance (Fig. 2). Further effects, such as doping inhomogeneity and band bending near surfaces were also neglected.

V. SUMMARY

We measured transient effective conductivity spectra in a regular array of heavily Sn-doped InP nanowires. We described the effective absorption of the excitation beam as a function of the excitation wavelength: the effective absorption is resonantly enhanced around 750 nm, and suppressed for shorter excitation wavelengths. The role of the depolarization fields was examined carefully, which enabled us to establish a link between the microscopic and effective conductivity spectra. Finally, Monte Carlo calculations of the electron response in heavily doped nanowires were developed and used for the determination of the electron scattering time in the nanowires. This time was found to be longer than ∼150 fs, corresponding to the transversal mobility exceeding 3000 cm^2 V^{-1} s^{-1}. The developed approach describes a relation between the charge mobility and quantities measurable by THz spectroscopy. It is an important step towards the solution of the inverse problem, i.e., direct determination of mobility in advanced semiconductor nanostructures from THz spectra measured in a noncontact way.

ACKNOWLEDGMENTS

This work was performed within the Nanometer Structure Consortium at Lund University (nmC@LU) and was supported by the Swedish Research Council (Vetenskapsrådet), by the Knut and Alice Wallenberg Foundation, by the Swedish Energy Agency, and by the Crafoord Foundation. This project was also supported by the Academy of Sciences of the Czech Republic under Project M100101218 and by the Czech Science Foundation under Grant 13-12386S.

APPENDIX A: DEFINITION OF EFFECTIVE ABSORPTION

There are several ways to define the effective absorption coefficient. One possibility (followed in the paper) is to define the effective absorption coefficient α_{eff} of the mixture of InP nanowires and PDMS matrix as the attenuation of the photon exposure per infinitesimal distance (averaged over entire surface). In certain situations, it is more convenient to introduce effective absorption coefficient normalized by the surface coverage of the nanowires ($\alpha'_{\mathrm{eff}} = \alpha_{\mathrm{eff}}/s$) which expresses the absorption per volume of the absorbing material. Using the latter definition, it is straightforward to define the absorption enhancement factor $\beta = \alpha'_{\mathrm{eff}}/\alpha = \alpha_{\mathrm{eff}}/(s\alpha)$ which compares the effective absorption with the absorption of the material α and which accounts for the fact that the absorbing material is diluted in the matrix array of nanowires.

One should also carefully distinguish between excitation density in the nanowires n_{exc} and the excitation density averaged over the sample cross-section n'_{exc}. These quantities differ by the factor s:

$$n_{\mathrm{exc}}(z) = H_{\mathrm{p}}\frac{\alpha_{\mathrm{eff}}}{s}\exp(-\alpha_{\mathrm{eff}}z) = H_{\mathrm{p}}\alpha'_{\mathrm{eff}}\exp(-s\alpha'_{\mathrm{eff}}z),$$
$$n'_{\mathrm{exc}}(z) = H_{\mathrm{p}}\exp(-\alpha_{\mathrm{eff}}z) = H_{\mathrm{p}}s\alpha'_{\mathrm{eff}}\exp(-s\alpha'_{\mathrm{eff}}z).$$

Note that the decay of the excitation density observed in Fig. 2(c) corresponds to the absorption coefficient α_{eff}, not to α'_{eff}.

In the finite-element calculations, we determined the transmission (t) and reflection (r) spectrum of the structure. The effective absorption α_{eff} then reads

$$\alpha_{\mathrm{eff}} = -\frac{\ln\frac{t}{1-r}}{L},$$

where L is the length of the nanowires.

APPENDIX B: LIST OF SYMBOLS

Input parameters	
$a = 500$ nm	distance between centers of nanowires in the array
$\alpha(\lambda_{\mathrm{exc}})$	spectrum of optical absorption coefficient of InP [29]
$d = 150$ nm	diameter of nanowires
$\varepsilon_{\mathrm{m}} = 2$	permittivity of polymer matrix at THz frequencies [30]
$\varepsilon_{\mathrm{NW}} = 12.5$	permittivity of InP nanowires at THz frequencies (equal to that of bulk InP) [10]
φ	quantum yield of electron generation (free parameter)
$K = 1$	depolarization factor of nanowires
$L = 1.3\ \mu$m	length of the nanowires (equivalent to the thickness of the photoconducting layer)
$m^* = 0.08m_{\mathrm{e}}$	effective mass of electrons in InP
$n = 2$	THz refractive index of the material surrounding the photoconducting layer
τ_{s}	electron mean scattering time (free parameter)
Other symbols	
e_0	elementary charge (positive)
H_{p}	photon exposure (variable)
λ_{exc}	excitation wavelength (variable)
$\Delta\sigma$	transient conductivity (response to the local THz field)
$\Delta\sigma_{\mathrm{eff}}$	transient effective conductivity (response to the applied THz field)
$\Delta\Sigma_{\mathrm{eff}}$	transient effective sheet conductivity
$\Delta T/T$	transient transmittance
ω	angular probing THz frequency (variable)
z	depth in the sample
Z_0	vacuum impedance
Derived quantities	
$\alpha_{\mathrm{eff}}(\lambda_{\mathrm{exc}})$	spectrum of effective optical absorption coefficient [Fig. 2(c)]
β	optical absorption enhancement factor [$=\alpha_{\mathrm{eff}}/(s\alpha)$]
$B = 0.0059$	constant in Eq. (3)
$D = 0.067$	constant in Eq. (3)
$E_{\mathrm{F}} \sim 0.25$ eV	Fermi energy of electrons in nanowires (calculated from the doping level 5×10^{18} cm^{-3})
$\varepsilon_{\mathrm{eff}} = 2.2$	effective permittivity of the polymer + nanowires layer (the value is low due to absence of percolation path in the direction of the electric field)
n_{exc}	excitation density, Eq. (1)
$s = 7\%$	surface coverage by the nanowires [$\pi d^2/4a^2$]

[1] R. Ulbricht, E. Hendry, J. Shan, T. F. Heinz, and M. Bonn, Rev. Mod. Phys. **83**, 543 (2011).

[2] D. Grischkowsky, S. Keiding, M. van Exter, and Ch. Fattinger, J. Opt. Soc. Am. B **7**, 2006 (1990).

[3] D. G. Cooke, A. N. MacDonald, A. Hryciw, J. Wang, Q. Li, A. Meldrum, and F. A. Hegmann, Phys. Rev. B **73**, 193311 (2006).

[4] K. Storm, F. Halvardsson, M. Heurlin, D. Lindgren, A. Gustafsson, P. M. Wu, B. Monemar, and L. Samuelson, Nat. Nanotechnol. **7**, 718 (2012).

[5] H. Němec, P. Kužel, and V. Sundström, Phys. Rev. B **79**, 115309 (2009).

[6] H. Němec, P. Kužel, and V. Sundström, J. Photochem. Photobiol. A **215**, 123 (2010).

[7] H.-K. Nienhuys and V. Sundström, Appl. Phys. Lett. **87**, 012101 (2005).

[8] E. Hendry, M. Koeberg, B. O'Regan, and M. Bonn, Nano Lett. **6**, 755 (2006).

[9] H. Němec, V. Zajac, I. Rychetský, D. Fattakhova-Rohlfing, B. Mandlmeier, T. Bein, Z. Mics, and P. Kužel, IEEE THz Sci. Technol. **3**, 302 (2013).

[10] H. J. Joyce, C. J. Docherty, Q. Gao, H. H. Tan, C. Jagadish, J. Lloyd-Hughes, L. M. Herz, and M. B. Johnston, Nanotechnology **24**, 214006 (2013).

[11] H. J. Joyce *et al.*, Nano Lett. **12**, 5325 (2012).

[12] P. Parkinson, C. Dodson, H. J. Joyce, K. A. Bertness, N. A. Sanford, L. M. Herz, and M. B. Johnston, Nano Lett. **12**, 4600 (2012).

[13] P. Parkinson, H. J. Joyce, Q. Gao, H. H. Tan, X. Zhang, J. Zou, C. Jagadish, L. M. Herz, and M. B. Johnston, Nano Lett. **9**, 3349 (2009).

[14] P. Parkinson, J. Lloyd-Hughes, Q. Gao, H. H. Tan, C. Jagadish, M. B. Johnston, and L. M. Herz, Nano Lett. **7**, 2162 (2007).

[15] J. Mrozek and H. Němec, Phys. Rev. B **86**, 075308 (2012).

[16] N. Anttu, Opt. Lett. **38**, 730 (2013).

[17] J. Wallentin, N. Anttu, D. Asoli, M. Huffman, I. Åberg, M. H. Magnusson, G. Siefer, P. Fuss-Kailuweit, F. Dimroth, B. Witzigmann, H. Q. Xu, L. Samuelson, K. Deppert, and M. T. Borgström, Science **339**, 1057 (2013).

[18] H. P. Porte, D. Turchinovich, S. Persheyev, Y. Fan, M. J. Rose, and P. U. Jepsen, IEEE THz Sci. Technol. **3**, 331 (2013).

[19] P. Kužel and H. Němec, J. Phys. D (to be published).

[20] H. Němec, J. Rochford, O. Taratula, E. Galoppini, P. Kužel, T. Polívka, A. Yartsev, and V. Sundström, Phys. Rev. Lett. **104**, 197401 (2010).

[21] M. T. Borgström, E. Norberg, P. Wickert, H. A. Nilsson, J. Trägardh, K. A. Dick, G. Statkute, P. Ramvall, K. Deppert, and L. Samuelson, Nanotechnology **19**, 445602 (2008).

[22] M. T. Borgström, J. Wallentin, J. Trägardh, P. Ramvall, M. Ek, L. R. Wallenberg, L. Samuelson, and K. Deppert, Nano Res. **3**, 264 (2010).

[23] J. Wallentin, M. Ek, L. R. Wallenberg, L. Samuelson, and M. T. Borgström, Nano Lett. **12**, 151 (2012).

[24] PDMS is a polymer transparent both in optical and THz range. Its optical refractive index used in the calculations was 1.41.

[25] Diffusion coefficient of bulk InP is 140 $\mathrm{cm}^2\,\mathrm{s}^{-1}$ at room temperature. The mean diffusion length $\sqrt{D\tau}$ at the time of $\tau = 10$ ps is then equal to 370 nm. The charge distribution density will be thus almost homogeneous in transverse planes and smoothly varying in the longitudinal direction.

[26] J. Wallentin, K. Mergenthaler, M. Ek, L. R. Wallenberg, L. Samuelson, K. Deppert, M.-E. Pistol, and M. T. Borgström, Nano Lett. **11**, 2286 (2011).

[27] L. Fekete, P. Kužel, H. Němec, F. Kadlec, A. Dejneka, J. Stuchlík, and A. Fejfar, Phys. Rev. B **79**, 115306 (2009).

[28] D. A. Anderson, N. Apsley, P. Davies, and P. L. Giles, J. Appl. Phys. **58**, 3059 (1985).

[29] S. Adachi, J. Appl. Phys. **66**, 6030 (1989).

[30] I. E. Khodasevych, C. M. Shah, S. Sriram, M. Bhaskaran, W. Withayachumnanku, B. S. Y. Ung, H. Lin, W. S. T. Rowe, D. Abbott, and A. Mitchell, Appl. Phys. Lett. **100**, 061101 (2012).